SPECIAL SECTION: EMERGING PARTICLES AND BIOCOLLOIDS
IN TERRESTRIAL AND AQUATIC SYSTEMS

Experimental quantification of interfacial convections at the water–nonaqueous-phase liquid interface in microfluidic systems

Carina Wismeth[1] | **Markus Flury**[2] | **Thomas Baumann**[3]

[1]Chair of Analytical Chemistry and Water Chemistry, Technical University of Munich, Institute of Hydrochemistry, Garching 85748, Germany

[2]Dep. of Crop & Soil Sciences, Puyallup Research & Extension Center, Washington State Univ., Puyallup, WA 98371, USA

[3]Chair of Hydrogeology, TUM School of Engineering and Design, Technical University of Munich, Munich 80333, Germany

Correspondence
Thomas Baumann, Chair of Hydrogeology, TUM School of Engineering and Design, Technical University of Munich, Munich, Germany, 80333.
Email: tbaumann@tum.de

Assigned to Associate Editor Christophe Darnault.

Abstract

Mass transfer rates at liquid–liquid interfaces are relevant for a broad range of processes in natural and technical systems. The objective of this study was to characterize and quantify convective flow along the interface between water and nonaqueous-phase liquids (NAPLs). Three NAPLs with different water solubility were used: 1-heptanol, 1-octanol, and 1-nonanol. The convective flow was visualized and recorded in a micromodel setup with fluorescent particles and an epifluorescence microscope. Individual trajectories were evaluated to obtain the statistics of the particle velocities. We observed a fast-rotating convection current along the NAPL–water interface with a maximum velocity of approximately 1,000 μm s^{-1} after 10 min. The fluid motion showed a persistent movement in the form of a rolling cell for at least 99 h, but a decreasing rotation speed over time. We attributed the convective flow dynamics to three mechanisms following different kinetic rates: (a) a short-lived Marangoni flow, (b) a medium-lived dissolution-driven flow, and (c) a long-lived evaporation-driven flow. Upon initial contact between water and NAPLs, the differences in surface tension caused a rapid Marangoni flow along the interface, which died out quickly as the surface tensions were equilibrated. The Marangoni flow was superseded by a dissolution-driven flow as the NAPLs dissolved in the aqueous phase. The dissolution-driven flow dissipated according to a first-order rate law and died out when the liquids were mutually saturated. Evaporation of water and NAPLs caused a long-term but slow convective flow. The interaction of these three mechanisms caused enhanced mixing during multiphase transport.

Abbreviations: NAPL, nonaqueous-phase liquid; PTFE, polytetrafluoroethylene.

1 | INTRODUCTION

Dissolution processes and mass transfer processes at fluid interfaces are generally considered to be dominated by diffusion (Eberhardt & Grathwohl, 2002). In a stagnant solution, for instance in capillaries in the vadose zone, the concentration difference along the interface is decreased over time by Brownian motion, and the diffusive flux can be described by Fick's first and second laws (Cussler, 2009). However, mass transfer processes at fluid interfaces can also be facilitated by interfacial convection, caused by local inhomogeneities and hydrodynamic instabilities along the interface (Javadi et al., 2014; Linde, 1984; Smith, 1966). Local fluctuations in temperature or concentration result in an interface tension gradient that causes a deformation of the interface itself (Thomson, 1855; Wang et al., 2016). If there is a surface tension gradient (Marangoni effect) along a fluid interface, a shear stress is generated that results in dissipative motion—for example, in the form of roll cells (Javadi et al., 2014; Schwarzenberger et al., 2014; Sherwood & Wei, 1957; Sternling & Scriven, 1959). In case of a dependence on temperature alone, this effect is called thermocapillary Marangoni effect (Davis, 1987; Levich & Krylov, 1969). Surface tension is highly affected by temperature; thus, evaporation and associated temperature gradients along a fluid interface can lead to thermophoretic movements and dissipative motion due to evaporative heat loss (Fanton & Cazabat, 1998; Flack et al., 2001; Hegseth et al., 1996; Spangenberg & Rowland, 1961). A decrease in the surface temperature can also result in an accompanying density increase, leading to a buoyancy-driven convection that is called Rayleigh–Bénard convection, which has been subject to considerable research (Cerbino et al., 2002; Köllner et al., 2016; Lappa, 2009). These interfacial convections that come along with an increased mixing of the phases can cause an increased mass transfer along the interface in a nonequilibrium, multiphase system (Loodts et al., 2017).

Besides convection driven by surface tension, dissolution processes of slightly soluble nonaqueous-phase liquids (NAPLs) are linked to local modifications of the fluid properties and interfacial dynamics, which also favor the development of interfacial convection (Loodts et al., 2017). Budroni et al. (2017) and Loodts et al. (2016, 2017) postulated that dissolution processes in partially miscible systems induce unstable density stratifications that favor convective dynamics. Depending on the host solution, this convective flow can exceed diffusive flow and becomes the dominant transport process. Dietrich et al. (2016) stated that interfacial convection currents around a sessile droplet in water can be induced by the dissolution of highly soluble alcohols. Convection rolls can be caused and controlled by hydrodynamic instabilities, friction forces along the interface, and

Core Ideas

- Mass transfer across interfaces is strongly affected by interfacial motion
- Interfacial motion is driven by Marangoni, dissolution-driven, and evaporation-driven flow.
- Enhanced mixing of phases is expected in the vadose zone at non-aqueous-phase liquids–water interfaces.

the overall process is postulated to be driven by buoyancy (Dietrich et al., 2016).

The objective of this study was to quantify the convection at fluid interfaces when a NAPL contacts an aqueous phase. We combined microfluidic experiments with quantitative particle tracking, providing information for interfacial processes as well as flow directions and velocities of interfacial convections. The quantification of the mass transfer at fluid interfaces requires detailed knowledge of the development of interfacial convection. The results of this study allow the parametrization of an interfacial convection current at interfaces to nonaqueous phases, as well as the decoding of the dynamics of the overall process of the considered three-phase system.

2 | MATERIALS AND METHODS

2.1 | Materials

Fluorescent carboxylate modified non-cross-linked polystyrene latex microspheres (Molecular Probes F-8823) were used to visualize and quantify the flow in the water phase. The diameter of the particles is 1.0 μm, the specific density is 1.055 g cm^{-3}, the specific negative surface charge is 0.0148 mmolc g^{-1}, the specific surface area is 5.7 × 10^4 cm^2 g^{-1}, the excitation maximum of the fluorophore is 505 nm, and the emission maximum is 515 nm (all data provided by Molecular Probes). The fluorescent particles were diluted with Milli-Q ultrapure water to a number concentration of 3.6 × 10^9 particles L^{-1}.

The NAPLs (1-heptanol, 1-octanol, and 1-nonanol) were 99.0% pure (Merck KGaA) and were used in their pure state in the experiments. These alcohols have similar surface tensions and aqueous diffusion coefficients but differ in their solubilities (Table 1). To exclude effects by dissolution of one phase into the other, 1-octanol and water were also used in their mutually saturated state. For mutual saturation, the water and 1-octanol at a 1:1 volume ratio were over-

T A B L E 1 Selected properties of the nonaqueous-phase liquids (NAPLs) used in this work

NAPL	Formula	Surface tension (at 20 ˚C)	Density (at 20 ˚C)[a]	Solubility in H$_2$O (at 25 ˚C)[b]	Diffusion coefficient in H$_2$O (at room temp.)[c]	Vapor pressure (at 20 ˚C)
		mN m^{-1}	g cm^{-3}	mol L^{-1}	m^2 s^{-1}	hPa
1-heptanol	C$_7$H$_{15}$OH	26.5[d]	0.822	0.0146	0.718×10^{-9}	0.50[a]
1-octanol	C$_8$H$_{17}$OH	27.6[e]	0.824	0.0038	0.667×10^{-9}	0.03[f]
1-nonanol	C$_9$H$_{19}$OH	28.5[g]	0.827	0.0010	0.625×10^{-9}	0.02[a]

[a]Sigma-Aldrich (2018).
[b]Kinoshita et al. (1958).
[c]Kovalchuk et al. (2002).
[d]Wolf (1959).
[e]Ye and Li (2012).
[f]Roth (2018).
[g]Lide (2003).

head shaken for 24 h and then separated with a separatory funnel.

2.2 | Surface tension and contact angle measurement

The surface tension of the unsaturated and mutually saturated phases was measured with the Wilhelmy plate method (Processor Tensiometer K100, KRÜSS). Air–liquid–solid contact angles of the liquids with a polytetrafluoroethylene (PTFE) surface were measured by the sessile drop method. For contact angle measurements, a drop of 3 µl was dispensed with a syringe and analyzed with the Young–Laplace equation by using a Drop Shape Analyzer DSA100 (KRÜSS). Measurements were made at 25 ˚C.

2.3 | Micromodel experiments

2.3.1 | Micromodel design

The micromodel used for tracking the water flow at the interface (Figure 1a) was designed to mimic the aspect ratio of pore bodies and pore throats. It consists of a larger reservoir for the water (pore body). The NAPL in the smaller reservoir is connected to the water reservoir through a rectangular channel (pore throat). The hydrophobic surface of PTFE prevents water to enter that channel while NAPLs are sucked into the channel by capillary forces. This allows for a well-defined geometry and initial condition of the experiments. Observation with an epifluorescence microscope (Olympus BX-60, Olympus) was from the top, and images were captured with a monochrome Genie HM 1024 CCD camera (resolution = 1,024 × 768 px; Teledyne DALSA) at a minimum frame rate of 10 frames s^{-1}.

The micromodel to measure dynamics of the Marangoni effect consisted of two equal reservoirs, which were connected by a small channel (Figure 1c,d). The water reservoir was covered by a housing to control relative humidity, and an additional water source ensured 100% humidity to prevent evaporation of the water droplet placed in one of the reservoirs. This setup allowed us to observe changes of the shape of the droplet in contact with different NAPLs with a camera that was horizontally mounted.

2.3.2 | Image acquisition and particle tracking

The image data were collected as a video stream with a frame rate of 20 frames s^{-1}. Particles were tracked by hand across the individual images using ImageJ (Schindelin et al., 2012; Schneider et al., 2012). Both the center of mass of the particle and the radius of the particle were used to track their motion at the interface and in the focal plane. The trajectory data (x,y coordinates, time, and trajectory identification) were used to calculate the velocity distribution in the focal plane. Up to 300 displacements of particles were evaluated for each test series. Figure 2 shows an example of calculated particle trajectories within the x,y focal plane (Figure 2a) and illustrates the position of the focal point of the microscope in relation to the recorded images (Figure 2b).

2.3.3 | Quantification of interfacial convection

To quantify particle velocities in the absence of a NAPL–water interface, the water reservoir (Figure 1a,b) was filled with 175 µl of the fluorescent particle suspension with a number concentration of 3.6 × 10^9 L^{-1}. A microscopy glass slide was placed loosely on the micromodel to reduce evaporation. It did not touch the water in the reservoir. The microscope was focused on the surface of the water drop. This
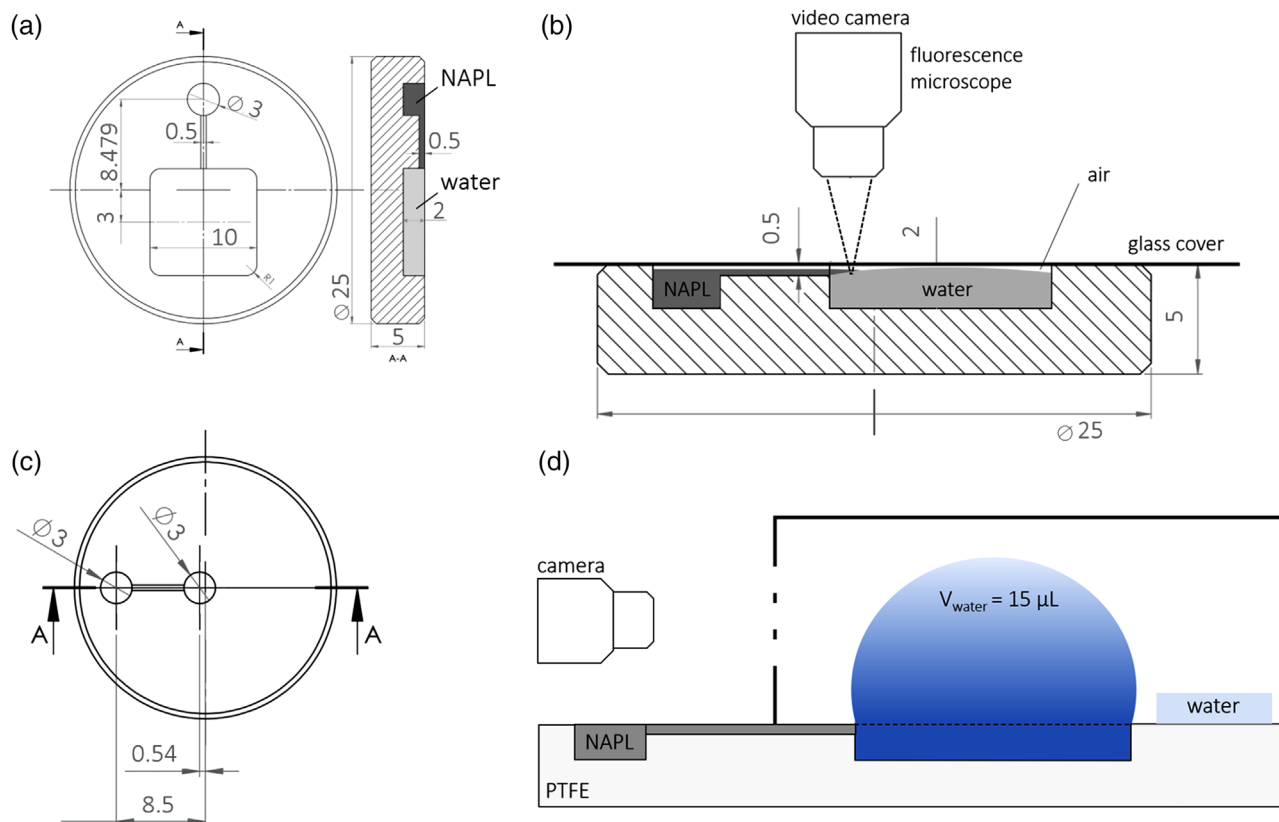
FIGURE 1 (a) Top view and side view of the micromodel with squared water reservoir; (b) experimental setup of the microscopic analysis; (c) top view and side view of the micromodel with cylindrical water reservoir; (d) experimental setup of the drop shape analysis. Dimensions are in millimeters. NAPL, nonaqueous-phase liquid; V_{water}, volume of water; PTFE, polytetrafluoroethylene; A, position of cross-section

background dataset presents undirected particle velocities due to Brownian motion in presence of evaporation but without a NAPL–water interface.

To quantify particle velocities in presence of a NAPL–water interface, the water reservoir was filled with 175 µl of the fluorescent particle suspension as described above, and then 10 µl of NAPL was added to the small NAPL reservoir (Figure 1b). In one set of experiments, a microscopy slide was attached to the PTFE surface with a polyester film to prevent evaporation; in another set of experiments, the glass slide was placed on the micromodel without adhesive to minimize, but not prevent evaporation. The epifluorescent microscope was always focused on the NAPL–water interface (Figure 1b), and images were recorded as described above. After adding the NAPL, the NAPL crept through the channel towards the water reservoir by capillary forces and created the fluid–fluid interface. As soon as the NAPL met the aqueous phase (time $t = 0$), a rotational motion of the fluorescent particles within the aqueous phase was observed and recorded. These data provided particle velocities in presence and absence of evaporation, and with a fresh NAPL–water interface. The experiments were repeated with mutually saturated 1-octanol and water, conducted in

the same way and with identical volumes as described above.

2.3.4 | Marangoni effect

When the NAPL contacts water, there will be a pronounced gradient in surface tension (Table 1). To quantify the effect of the surface tension differences, we measured the dynamics of the surface tension when the NAPL contacted the water phase. As it is difficult to directly measure surface tension in our micromodel because of its small size, we determined the surface tension indirectly by measuring the contact angle of the water drop against the micromodel surface. For that purpose, we used the micromodel shown in Figure 1c, which consists of a cylindrical water reservoir. A 15-µl drop of water was placed into the water reservoir, causing the drop to protrude out of the reservoir as shown in Figure 1d. A humidity-control chamber equipped with two glass windows at each side was used to minimize evaporation (Figure 1d). Two water-filled cups were placed into the humidity chamber to keep the atmosphere inside the chamber close to 100% relative humidity. Preliminary tests showed that the water drop remained con-
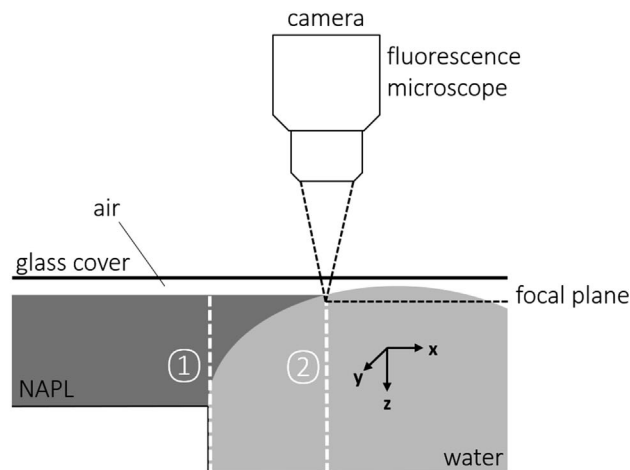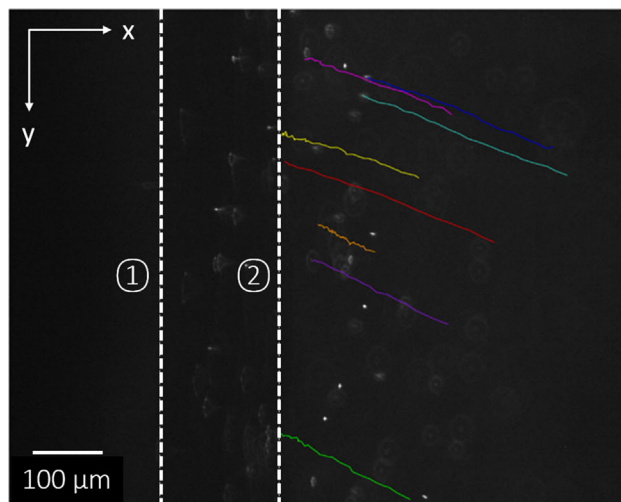
FIGURE 2   Left: Trajectories of single particles within the aqueous phase during their movement within the focal plane (top view on the x,y plane) in the octanol–water system. Right: Schematic of the configuration of the nonaqueous-phase liquid (NAPL)–water interface illustrating the focal point

stant and indeed did not evaporate during the duration of the experiments (1 h). The contact angle of the water drop against the PTFE surface was measured with a Drop Shape Analyzer DSA100 (KRÜSS). The drop shape and contact angles were recorded in 10-min intervals for a total duration of 1 h.

The measurements were started as soon as the NAPL was placed into the NAPL reservoir. The NAPL crept through the channel and then contacted the water drop. Supplemental Figure S1 illustrates the geometry of the system and the contact angles measured. The edge of the cylindrical water reservoir (90˚) causes the air–water interface to get pinned and leads to a contact angle that can exceed the equilibrium contact angle (Chatterjee & Flury, 2013; Singh & Joseph, 2005). The range of the contact angle of a pinned interface can be calculated with the Gibbs extension of the Young equation (Singh & Joseph, 2005) (see Supplemental Section S1 for details).

3 | RESULTS

3.1 | Surface tensions of water, NAPLs, and mutually saturated phases and contact angles with PTFE

The results of the surface tension measurements of the pure and mutually saturated phases are shown in Table 2 and are in agreement with the literature (Wolf, 1959). The contact angles shown in Table 2 are measured on a PTFE substrate. The contact angle and surface tension values of pure NAPLs and NAPLs saturated with water (superscript b) showed no

TABLE 2   Contact angles (liquid volume = 3 µl) on a polytetrafluoroethylene (PTFE) substrate and surface tension of the pure and mutually saturated aqueous phase and nonaqueous-phase liquids (NAPLs) (at 25 ˚C)

Liquid	Contact angle at PTFE	Surface tension
	degrees	mN m^{-1}
Pure phases		
Water	108.8 ± 0.8	72.5 ± 0.003
1-Heptanol	43.4 ± 0.3	26.6 ± 0.002
1-Octanol	40.9 ± 0.7	27.5 ± 0.005
1-Nonanol	42.3 ± 1.4	27.8 ± 0.005
Saturated phases		
Water/1-heptanol[a]	70.6 ± 0.6	29.1 ± 0.015
Water/1-octanol[a]	70.5 ± 0.5	28.7 ± 0.007
Water/1-nonanol[a]	71.0 ± 1.1	27.0 ± 0.080
1-Heptanol/water[b]	44.5 ± 0.1	26.4 ± 0.008
1-Octanol/water[b]	41.3 ± 0.5	27.1 ± 0.006
1-Nonanol/water[b]	43.9 ± 1.0	27.5 ± 0.016

Note. Contact angles were measured with sessile drop method on a flat PTFE substrate. Data are means and standard deviations ($n = 10$).

[a] Water saturated with heptanol, octanol, or nonanol.

[b] Heptanol, octanol, or nonanol saturated with water.

significant differences. In contrast, the contact angle of water was reduced from 109˚ to 71˚ when the water was saturated with one of the NAPLs. Likewise, the surface tension of water saturated with one of the NAPLs was reduced from 73 to 27–29 mN m^{-1}, which is close to values of pure NAPLs.

T A B L E 3 Contact angle of the aqueous phase (pinned air–water interface) before and after adding the nonaqueous-phase liquid (NAPL) in the micromodel with the spherical reservoirs

| Time | Contact angle | | |
	Water/1-heptanol	Water/1-octanol	Water/1-nonanol
min	————————degrees————————		
Initial (pure water)[a]	186.3	187.1	186.2
0 (contact with NAPL)[b]	154.7	155.3	154.7
10	154.3	153.3	152.6
20	153.0	152.7	151.3
30	152.7	152.0	150.2
40	152.0	151.3	149.8
50	152.0	150.7	148.1
60	151.7	150.3	148.6
Water$_{NAPLsaturated}$	152.9	152.6	151.3

Note. The contact angle is measured as the angle within the aqueous phase, with respect to the vertical wall of the reservoir, including the wedge angle of 90°.

[a]Drop was pinned at the edge of the micromodel reservoir, so this contact is different than the 109° contact angle on a flat polytetrafluoroethylene (PTFE) surface (see Table 2).

[b]Upon contact with the NAPL, the drop detached from the wedge and formed a new contact angle on the horizontal portion of the micromodel. For comparison with the water contact angle, the reported contact angle is the angle with respective to the vertical wall of the reservoir.

3.2 | Surface tension gradient

The results of the time-dependent contact angle measurements of the aqueous phase upon contact with the NAPL are shown in Table 3 (see Supplemental Video S1). The contact angle measured is the angle between the air–liquid interface and the vertical PTFE surface or the reservoir from which the drop protrudes.

The results show that there is a rapid decrease by 30° immediately after the NAPL came into contact with the water droplet. This change of contact angle upon contact of the NAPL with the water is a consequence of the change of the aqueous phase surface tension. Later on, the contact angle remained fairly constant, with a slight decrease of contact angle with time, which might be caused by the evaporation of the liquid.

The measured contact angle after contact of NAPL with water is similar to the contact angle of the NAPL-saturated aqueous phase (Table 3). The contact angle of the saturated aqueous phase was measured in the same cylindrical reservoir with an identical volume of 15 μl without adding the corresponding NAPL.

The measured contact angle of the pure aqueous phase in the spherical reservoir (186°) exceeded the equilibrium contact angle of water on the PTFE substrate (108°). As the liquid drop protrudes out of the micromodel, the drop is pinned at the corner of the micromodel (Figure 1d; Supplemental Figure S1a), which allows the contact angle to exceed the equilibrium angle for a flat surface (Chatterjee & Flury, 2013; Flury & Aramrak, 2017; Singh & Joseph, 2005) (see Supplemental Section S1). Upon contact with the NAPL, however, the surface tension and the equilibrium contact angle on a flat surface decreased, leading the contact angle of the pinned interface at the edge of the micromodel to exceed the Gibbs relation (Singh & Joseph, 2005), and the drop slipped over the edge and established a new equilibrium on the horizontal surface of the micromodel (see Supplemental Section S1). The actual contact angle after detachment from the wedge, which is the angle reported in Table 3 minus the wedge angle of 90°, was 61–63° for the NAPL-saturated aqueous phases. This is smaller than the angle of $71 \pm 1°$ measured on a flat PTFE surface for the NAPL-saturated aqueous phases (Table 2) and indicates the presence of a thin film of the NAPL on the water phase.

3.3 | Micromodel experiments: Cellular interfacial convection

In the absence of NAPL, no directed movement and convective current was observed within the aqueous phase. Instead, solely the Brownian motion of the particles was recorded. In the presence of NAPLs, a strong interfacial convection within the aqueous phase was observed as soon as the NAPL contacted the water phase, as indicated by the motion of the fluorescent particles. The particles rose along the interface and moved into main water reservoir, downwards and out of the focal plane at a distance of around 500 μm to reappear along the interface again. Although the full convection roll cell could not be tracked in the video streams because the particles moved out of focus, the existence of a roll cell was verified by following particles manually in complementing experiments. The axis of the convection was horizontal, parallel to the interface, and the direction of the flow was the same for the entire test series. The recorded upward fluid motion along the NAPL–water interface is illustrated in Figure 3.

The focal plane of the microscope was set to the very top of the fluid phases, just below the glass slide, and so the particles showed a halo while moving upwards along the interface that decreased the closer they got to the focal plane. As soon as the particles entered the focal plane, they appeared as bright spots that enabled the particle tracking. This phenomenon is shown in Figure 4, where the apparent radius of the particles is plotted as a function of position.
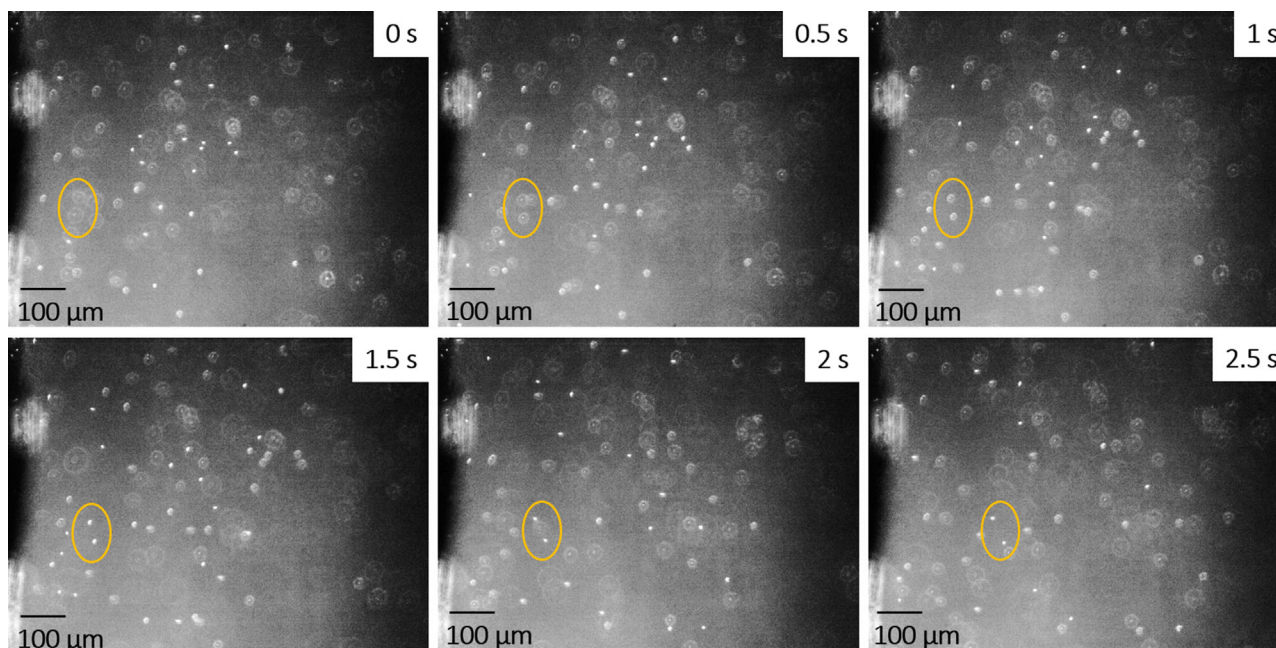
FIGURE 3 Series of pictures illustrating the upward fluid motion along the interface within the aqueous phase. The highlighted particles start blurry close to the interface to the nonaqueous-phase liquid (NAPL) (black without particles), which is at the left edge of the videographs. The particles come into focus (1.5 s) while moving only a little to the right. Once at the top of the interface, the particles stay in focus and move to the right (1.5–2.5 s). At the right edge of the videographs, a similar effect can be observed, but this time with particles moving right and out of focus
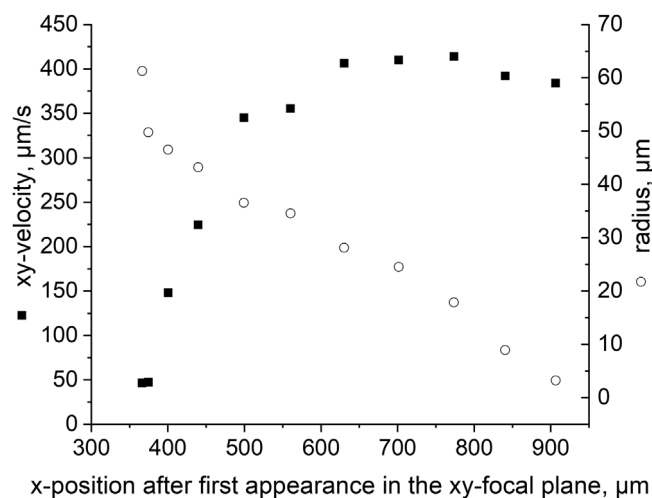
FIGURE 4 Comparison of the *xy* velocity and the change in radius of a single particle plotted against the distance of the particle from the interface in the 1-octanol–water system (1 h after joining the fluids)

3.4 | Dynamics of interfacial convection

3.4.1 | Interfacial velocities

The recorded velocities of the fluid motion along the NAPL–water interface showed an exponential decrease over time.

Within the first 10 min, the tracked particle velocity (= fluid motion along the interface) was the highest, and the particles appear as streaks that were longer than the field of view of the microscope even at maximum frame rate. Hence, the measurement of the velocities was impossible for the first seconds of the experiment. After that, an exact measurement was possible. Figure 5 shows the temporal change of the velocity of the interfacial convection in the system with 1-octanol from 10 min to 99 h. The velocity decreased from 1,050 to 330 μm s^{-1} after 10 min and to 230 μm s^{-1} after 3 h. After 99 h, the convection reached an equilibrium velocity of 30 μm s^{-1}.

We fitted the data with a first-order kinetics model (exponential model) and a two-stage first-order kinetics model. The overall process could not be well fitted with only one kinetic rate (Figure 5, blue solid line). However, the data could be better fitted with a two-stage first-order kinetics model that describes the overall process with two superposed exponential models with different time constants (Figure 5, red solid line). The fitting parameters are given in the corresponding equations in Figure 5, and the characteristic decay times for the two first-order processes are 0.23 and 15 h. The data also indicate that the velocity of the interface convection does not approach zero even after 99 h, but shows a constant offset (30 μm s^{-1}) that is much higher than the velocity from the unidirectional Brownian motion (3 μm s^{-1}).
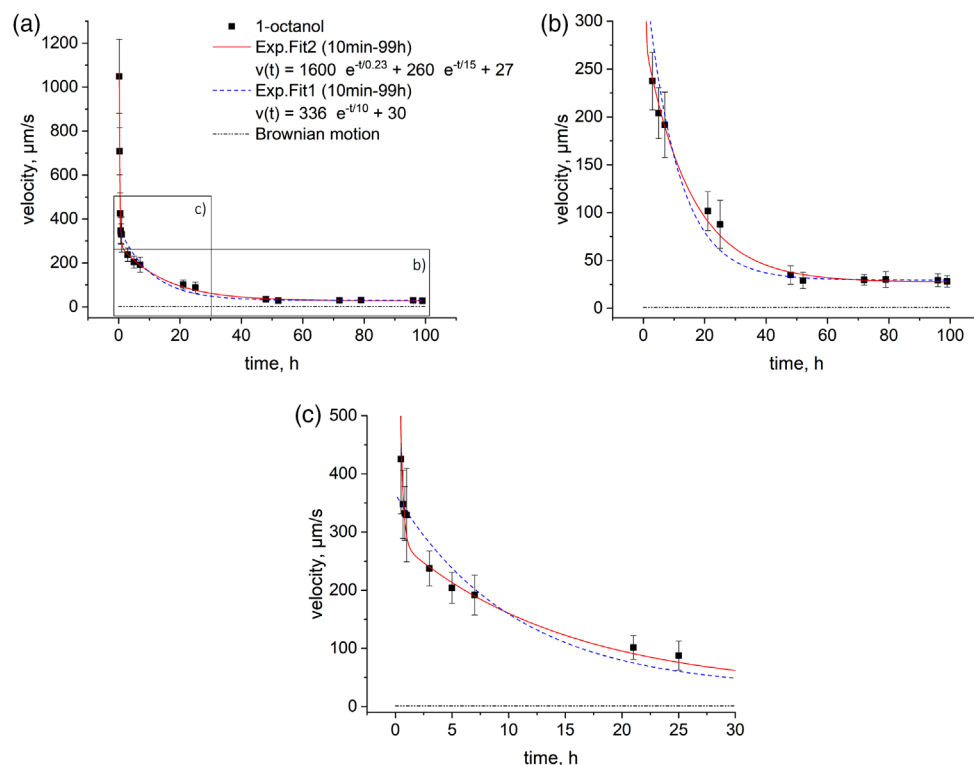
FIGURE 5 (a) Dynamics of the velocity of the directional movement of the fluorescent particles up to 99 h in the 1-octanol–water system (the symbols represent the mean of the calculated velocity with $n = 20$; the bars are the corresponding standard deviations; the red solid line is a two-stage exponential fit to the data from 10 min to 99 h; the blue dashed line is a one-stage exponential fit to the data from 10 min to 99 h; the corresponding fitted equations are given in the legend). (b and c) Enlarged sections of the black boxes indicated in (a). The black dashed-dotted line represents the initial velocity (3 μm s^{-1}) of the Brownian motion in the absence of the nonaqueous-phase liquid (NAPL)

3.4.2 | Effect of dissolution process

To investigate the effect of the dissolution of the NAPL in the aqueous phase, we determined the particle velocities in the micromodel for different NAPLs with different solubilities. The particle velocities were higher for the NAPLs that had a higher solubility in water, and the velocities ranked accordingly as heptanol > octanol > nonanol (Figure 6a). As the surface tensions of these NAPLs are similar (Table 1) and the NAPL-saturated surface tensions are also similar (Table 2), the different particle velocities must be related to the differences in solubilities of these NAPLs. When the two phases were mutually saturated, we did not observe a convective flow of the particles, and the velocities were low and constant (Figure 6b). The tracked particle velocities in the experiments with the three different NAPLs support the hypothesis of a dissolution-driven flow that takes over after the Marangoni flow dies out. The system with 1-heptanol, which has a higher solubility than 1-octanol, showed a higher velocity of the interfacial convection, whereas 1-nonanol, which has a lower solubility than 1-octanol, showed the lowest particle velocity. Within an experimental duration of 1 h, the velocity in the system with 1-heptanol decreased by 79.1% from 1,650 to

345 μm s^{-1}, the system with 1-octanol decreased by 83.1%, and the system with 1-nonanol decreased by 88.2%.

The experimental data could be well described with a first-order kinetics (Figure 6a) with characteristic decay times correlating well with the aqueous solubilities and diffusion coefficients of the NAPLs (Figure 6c,d). This further supports the hypothesis that the observed convection at this time scale is driven by dissolution of the NAPLs in the aqueous phase.

3.4.3 | Effect of evaporation

To investigate the impact of evaporation of the fluids on the velocity of the interfacial convection, the experiments were run with a sealed and unsealed system. A comparison of the convection velocities in the sealed and unsealed 1-octanol-water system for the time period between 1 and 7 h is shown in Figure 7. The data indicate that the evaporation of the aqueous phase had a strong impact on the velocity of the interfacial convection. After only 1 h, the sealed system shows a 21% lower velocity than the unsealed system. The unsealed system showed an overall decrease of the velocity by 23%, the velocity in the sealed system decreased by 99%.
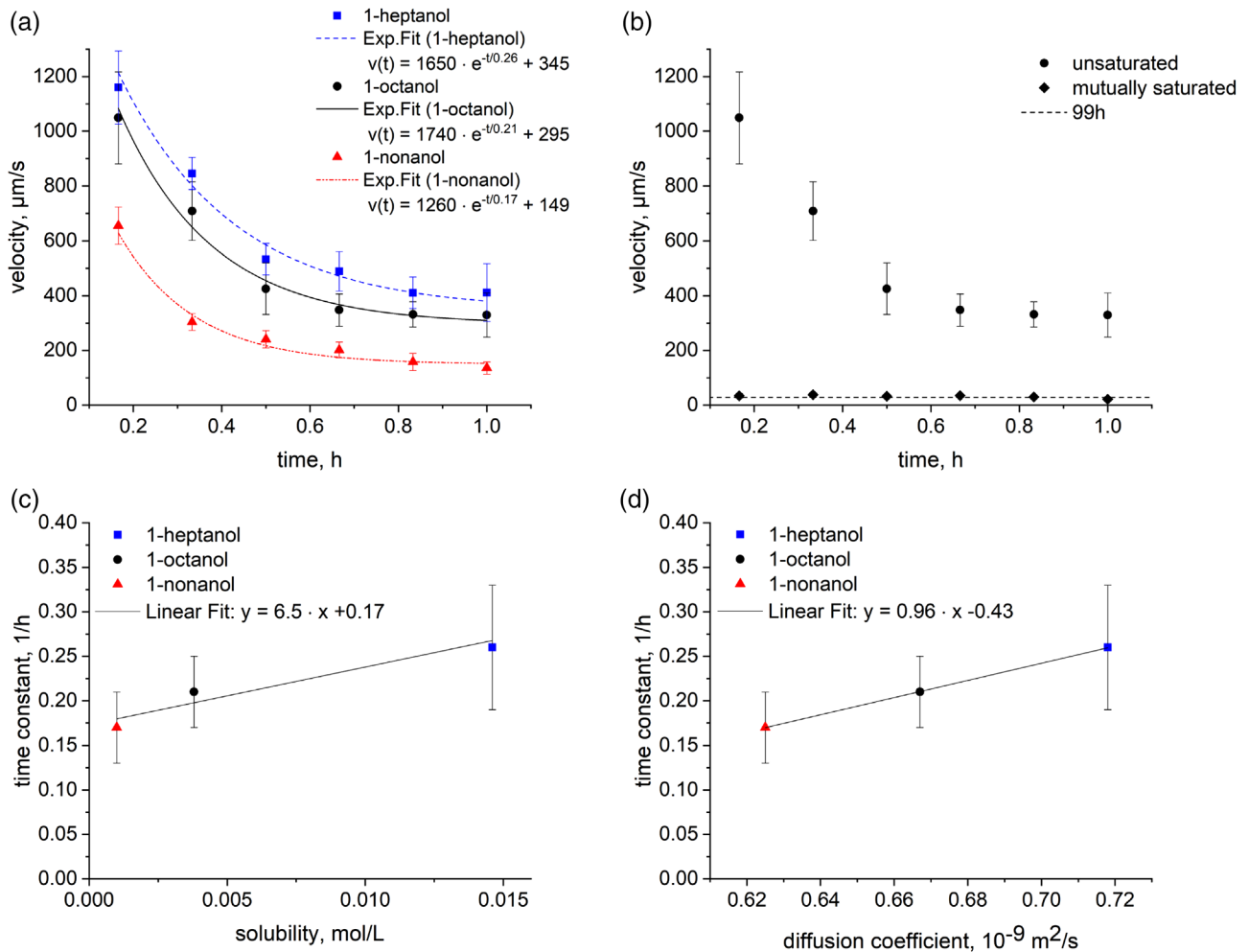
FIGURE 6 (a) Impact of the solubility of the nonaqueous-phase liquid (NAPL) on the velocity of the interfacial convection. (b) Comparison of the velocity of the interfacial convection in the unsaturated 1-octanol–water system and the mutually saturated 1-octanol–water system. The dashed line indicates the tracked velocity after 99 h in the 1-octanol–water system. (c) Correlation between the time constants and the solubilities of the NAPLs. (d) Correlation between the time constants and the diffusion coefficients of the NAPLs. Symbols represent the mean of the calculated velocity with $n = 20$; the bars are the corresponding standard deviations

4 | DISCUSSION

4.1 | Mechanisms of interfacial convection

The experimental data and the data analyses with first-order models suggest the presence of three different mechanisms causing the dynamics of the interfacial convection: (a) a fast-decaying Marangoni flow that dominates the early stage, (b) a slow-decaying dissolution-driven flow, and (c) a long-lasting evaporation-driven flow. The three mechanisms are schematically represented in Figure 8 and discussed in detail below.

4.2 | Surface tension driven flow

The reason for the rapid change of the surface tension of the aqueous phase owing to the addition of the NAPL is its

surface activity. As the long-chain alcohols show an amphiphilic molecular structure, they form a monolayer on the water surface (Donahue & Bartell, 1952). The wetting of the water surface with the alcohol molecules causes a surface tension gradient along the water surface (Figure 8a). This directed surface tension gradient causes interfacial instabilities that induce compensating currents and dissipative structures leading to Marangoni convection. The directed movement of the NAPL molecules along the water surface results in a strong interfacial drag force causing an ascending motion within the aqueous phase. The results of the trajectory analysis support this upward fluid motion of the fluorescent particles along the NAPL–water interface. As soon at the NAPL contacted the aqueous phase, a short-term wavy motion of the NAPL–water interface was observed (Supplemental Video S2), supporting the occurrence of an interfacial instability as well as a rapid change in the free energy of the system. Based on these results, we conclude that the onset of
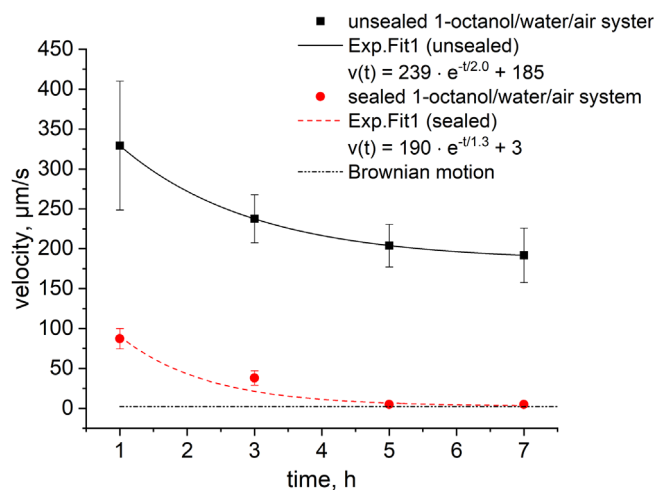
FIGURE 7 Comparison of the velocity of the interfacial convection in the unsealed system (black) and sealed octanol–water system (red). Symbols represent the mean of the calculated velocity with $n = 20$; the bars are the corresponding standard deviations. The dashed-dotted line represents the initial velocity ($3 \ \mu m \ s^{-1}$) of the Brownian motion in the absence of the nonaqueous-phase liquid (NAPL)

the convection is controlled by an initial surface tension driven Marangoni flow.

The contact angle analysis does indicate a rapid change in contact angle when the two phases contacted each other, but no significant change over time after that, and the contact angle approaches the contact angle of the saturated aqueous phases within a few seconds. That leads us to the conclude that the Marangoni effect dominates the dynamics only within the early stage and dissipates rapidly. As soon as the surface of the aqueous phase is completely saturated with alcohol molecules, there is no directed surface tension gradient anymore, and the convectional motion should also cease. The data in Figure 5, however, indicate an additional driving force that sustains the motion at later stages.

4.3 | Dissolution-driven flow

We attribute the longer lasting interfacial convection to the ongoing dissolution process of the NAPLs. This is supported by the pronounced differences in convective velocities for the different NAPLs, with the velocities being higher with higher solubility of the NAPLs. The surface tensions and densities of these NAPLs were similar, but their aqueous solubilities differed considerably (Table 1), so that we infer dissolution as the main driving force of the interfacial convection.

Due to the high velocities of about 1,000 $\mu m \ s^{-1}$ of the interfacial convection, we can assume that the ongoing dissolution process of the slightly soluble NAPLs exceeds the time scales of the surface tension driven flow, and thus dissolution-driven flow becomes the dominant process (Figure 8b). The cross-sectional view of the NAPL–water interface shows that the thickness of the NAPL is thinning out as it spreads over the water. Due to the smaller volume of the NAPL at the tip of the interface, a convective flow towards that region is induced. The direction of the flow is from the NAPL pool to the top of the film, generating additional drag forces that sustain the fluid motion along the interface within the aqueous phase. The resulting interfacial convection matches the recorded ascending motion direction in the aqueous phase. In absence of dissolution (i.e., when we ran the experiments with mutually saturated liquids), we also observed a directional convection, but with a much smaller velocity than when pure solutions were used. This indicates the presence of a third sustaining force that keeps the convection going after the solutions were mutually saturated and prevents the directional motion to cease.

4.4 | Evaporation-driven flow

A sustained directional motion was still observed after the liquids were mutually saturated, and we attribute the driving force of this motion to evaporation of the aqueous phase. When we sealed the micromodel and evaporation was prevented, the directional motion stopped and only the random Brownian motion was observed. This suggests that the directional motion in the unsealed system is due to evaporation of the aqueous phase rather than that of the NAPLs, because the NAPLs have a vapor pressure three to four orders of magnitude smaller than that of water (Table 1). The evaporation of the aqueous phase at the top of the micromodel induces a temperature gradient along the interface due to latent heat loss that results in a thermophoretic movement (Chai & Zhang, 1998; Fanton & Cazabat, 1998; Flack et al., 2001; Hegseth et al., 1996; Saylor et al., 2000) (Figure 8c). The decreased surface temperature at the apex of the aqueous phase increases the fluid density, which leads to a downward movement of the colder and more dense fluid. This buoyancy driven convection is called Rayleigh–Bénard convection and has been subject to considerable research (Cerbino et al., 2002; Köllner et al., 2016; Lappa, 2009). In addition, the temperature gradient along the NAPL–water interface caused a surface tension gradient, inducing a Marangoni flow. Buoyancy and surface tension driven flow often work in combination (Köllner et al., 2016, 2017; Nield, 1964; Pantaloni et al., 1979; Sun et al., 2002; Villers & Platten, 1992). Our experimen-
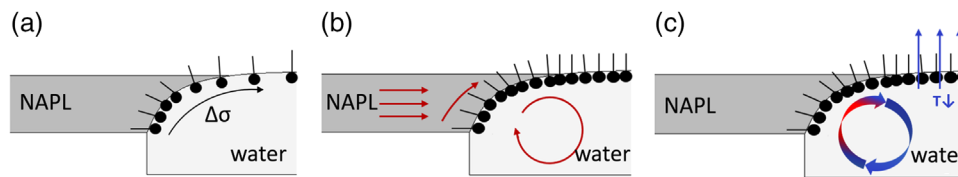
FIGURE 8 Schematic representation of the three dominating mechanisms causing interfacial convection when a nonaqueous-phase liquid (NAPL) contacts an aqueous phase: (a) directed surface tension gradient along the surface of the aqueous phase, (b) shear force along the NAPL–water interface due to dissolution, and (c) evaporation-induced temperature gradient along the saturated interface. The long straight arrows indicate the higher evaporation of the aqueous phase leading to a temperature decrease

tal results indicate that after the dissolution-driven flow tails off due to saturation of the phases, the evaporation and the accompanying thermophoretic effect sustain the fluid motion and result in a constant, nondecaying velocity at later stages.

5 | IMPLICATIONS

Interfacial dynamics and nonequilibrium are the driving forces for interfacial flows that affect mass transfer at fluid interfaces. Strong convective interfacial currents can develop along interfaces between NAPLs and water when the two liquids meet. Such interfacial currents induce convective flows within the liquids, which lead to enhanced mixing and mass transfer. In this study, we identified three main mechanisms of the convective flow, each with distinct kinetic rates: (a) a fast-decaying surface-tension-driven flow that dominates the early stage (Marangoni convection), (b) a sustaining but decaying dissolution-driven flow that follows a first-order exponential decay, and (c) an evaporative-driven flow that sustains the fluid motion and follows a linear kinetics.

These findings have some important implications for the fate of NAPLs in contaminated soils or sediments. In soils or sediments, evaporative-driven flow will only play a dominant role when the NAPL contamination occurs close to the soil surface where evaporation is possible. Deeper in the soil profile, however, evaporation will be minimal and the vapor phase will be close to the saturated vapor pressure of the individual phases. In this case, the convective currents will die out fairly quickly (i.e., within a couple of hours) but nonetheless help to facilitate mixing of the aqueous and nonaqueous phases. A likely scenario in which interfacial motion at NAPL–water interfaces is important is heavy rainfall after longer droughts. Here, the roll cells at the NAPL interfaces can increase the mass transfer to values well above the theoretical values based on a diffusive release.

AUTHOR CONTRIBUTIONS
Carina Wismeth: Formal analysis; Investigation; Methodology; Project administration; Validation; Visualization; Writing – original draft. Markus Flury: Formal analysis; Funding acquisition; Methodology; Resources; Software; Validation; Visualization; Writing – review & editing. Thomas Baumann: Conceptualization; Funding acquisition; Methodology; Resources; Software; Supervision; Validation; Visualization; Writing – review & editing.

ORCID
Markus Flury https://orcid.org/0000-0002-3344-3962
Thomas Baumann https://orcid.org/0000-0002-0934-2715

REFERENCES
Budroni, M. A., Thomas, C., & De Wit, A. (2017). Chemical control of dissolution-driven convection in partially miscible systems: Nonlinear simulations and experiments. *Physical Chemistry Chemical Physics*, *19*, 7936–7946. https://doi.org/10.1039/C6CP08434F

Cerbino, R., Vailati, A., & Giglio, M. (2002). Soret driven convection in a colloidal solution heated from above at very large solutal Rayleigh number. *Physical Review E*, *66*, 055301. https://doi.org/10.1103/PhysRevE.66.055301

Chai, A.-T., & Zhang, N. (1998). Experimental study of Marangoni-Benard convection in a liquid layer induced by evaporation. *Experimental Heat Transfer*, *11*, 187–205. https://doi.org/10.1080/08916159808946561

Chatterjee, N., & Flury, M. (2013). Effect of particle shape on capillary forces acting on particles at the air-water interface. *Langmuir*, *29*, 7903–7911. https://doi.org/10.1021/la4017504

Cussler, E. C. (2009). *Diffusion: Mass transfer in fluid systems*. Cambridge University Press.

Davis, S. H. (1987). Thermocapillary instabilities. *Annual Review of Fluid Mechanics*, *19*, 403–435. https://doi.org/10.1146/annurev.fl.19.010187.002155

Dietrich, E., Wildeman, S., Visser, C. W., Hofhuis, K., Kooij, E. S., Zandvliet, H. J. W., & Lohse, D. (2016). Role of natural convection in the dissolution of sessile droplets. *Journal of Fluid Mechanics*, *794*, 45–67. https://doi.org/10.1017/jfm.2016.158

Donahue, D. J., & Bartell, F. E. (1952). The boundary tension at water-organic liquid interfaces. *Journal of Physical Chemistry*, *56*, 480–484. https://doi.org/10.1021/j150496a016

Eberhardt, C., & Grathwohl, P. (2002). Time scales of organic contaminant dissolution from complex source zones: Coal tar pools vs. blobs. *Journal of Contaminant Hydrology*, *59*, 45–66. https://doi.org/10.1016/S0169-7722(02)00075-X

Fanton, X., & Cazabat, A. M. (1998). Spreading and instabilities induced by a solutal Marangoni effect. *Langmuir*, *14*, 2554–2561. https://doi.org/10.1021/la971292t

Flack, K. A., Saylor, J. R., & Smith, G. B. (2001). Near-surface turbulence for evaporative convection at an air/water interface. *Physics of Fluids*, *13*, 3338–3345. https://doi.org/10.1063/1.1410126

Flury, M., & Aramrak, S. (2017). Role of air-water interfaces in colloid transport in porous media: A review. *Water Resources Research*, *53*, 5247–5275. https://doi.org/10.1002/2017WR020597

Hegseth, J. J., Rashidnia, N., & Chai, A. (1996). Natural convection in droplet evaporation. *Physical Review E*, *54*, 1640–1644. https://doi.org/10.1103/PhysRevE.54.1640

Javadi, A., Karbaschi, M., Bastani, D., Ferri, J. K., Kovalchuk, V. I., Kovalchuk, N. M., Javadi, K., & Miller, R. (2014). Marangoni instabilities for convective mobile interfaces during drop exchange: Experimental study and CFD simulation. *Colloids and Surfaces A: Physicochemical and Engineering Aspects*, *441*, 846–854. https://doi.org/10.1016/j.colsurfa.2012.10.032

Kinoshita, K., Ishikawa, H., & Shinoda, K. (1958). Solubility of alcohols in water determined by the surface tension measurements. *Bulletin of Chemical Society of Japan*, *31*, 1081–1082. https://doi.org/10.1246/bcsj.31.1081

Köllner, T., Boeck, T., & Schumacher, J. (2017). Thermal Rayleigh-Marangoni convection in a three-layer liquid-metal-battery model. *Physical Review*, *95*, 053114.

Köllner, T., Schwarzenberger, K., Eckert, K., & Boeck, T. (2016). The eruptive regime of mass-transfer-driven Rayleigh-Marangoni convection. *Journal of Fluid Mechanics*, *791*, 1–12.

Kovalchuk, N. M., Kovalchuk, V. I., & Vollhardt, D. (2002). Auto-oscillations of surface tension: Experiments with octanol and hexanol and numerical simulation of the system dynamics. *Colloids and Surfaces A: Physicochemical and Engineering Aspects*, *198*, 223–230. https://doi.org/10.1016/S0927-7757(01)00934-7

Lappa, M. (2009). *Thermal convection: Patterns, evolution and stability*. John Wiley & Sons.

Levich, V. G., & Krylov, V. S. (1969). Surface-tension-driven phenomena. *Annual Review of Fluid Mechanics*, *1*, 293–316. https://doi.org/10.1146/annurev.fl.01.010169.001453

Lide, D. R. (2003). *Handbook of chemistry and physics* (Vol. 53, 84th ed.) CRC Press.

Linde, H. (1984). Time-dependent behaviour and regularity of dissipative structures of interfacial dynamic instabilities. *Faraday Discussions of the Chemical Society*, *77*, 181–188. https://doi.org/10.1039/dc9847700181

Loodts, V., Knaepen, B., Rongy, L., & De Wit, A. (2017). Enhanced steady-state dissolution flux in reactive convective dissolution. *Physical Chemistry Chemical Physics*, *19*, 18565–18579. https://doi.org/10.1039/C7CP01372H

Loodts, V., Trevelyan, P. M. J., Rongy, L., & De Wit, A. (2016). Density profiles around reaction-diffusion fronts in partially miscible systems: A general classification. *Physical Review E*, *94*, 043115. https://doi.org/10.1103/PhysRevE.94.043115

Nield, D. A. (1964). Surface tension and buoyancy effects in cellular convection. *Journal of Fluid Mechanics*, *19*, 341–352. https://doi.org/10.1017/S0022112064000763

Pantaloni, J., Bailleux, R., Salan, J., & Velarde, M. G. (1979). Rayleigh-Benard-Marangoni instability: New experimental results. *Journal of Non-Equilibrium Thermodynamics*, *4*, 201. https://doi.org/10.1515/jnet.1979.4.4.201

Roth, C. (2018). *1-octanol manufacturer information*.

Saylor, J. R., Smith, G. B., & Flack, K. A. (2000). The effect of a surfactant monolayer on the temperature field of a water surface undergoing evaporation. *International Journal of Heat and Mass Transfer*, *43*, 3073–3086. https://doi.org/10.1016/S0017-9310(99)00356-7

Schindelin, J., Arganda-Carreras, I., Frise, E., Kaynig, V., Longair, M., Pietzsch, T., Preibisch, S., Rueden, C., Saalfeld, S., Schmid, B., Tinevez, J.-Y., White, D. J., Hartenstein, V., Eliceiri, K., Tomancak, P., & Cardona, A. (2012). Fiji: An open-source platform for biological-image analysis. *Nature Methods*, *9*, 676–682. https://doi.org/10.1038/nmeth.2019

Schneider, C. A., Rasband, W. S., & Eliceiri, K. W. (2012). NIH Image to ImageJ: 25 years of image analysis. *Nature Methods*, *9*, 671–675. https://doi.org/10.1038/nmeth.2089

Schwarzenberger, K., Köllner, T., Linde, H., Boeck, T., Odenbach, S., & Eckert, K. (2014). Pattern formation and mass transfer under stationary solutal Marangoni instability. *Advances in Colloid and Interface Science*, *206*, 344–371. https://doi.org/10.1016/j.cis.2013.10.003

Sherwood, T., & Wei, J. (1957). Interfacial phenomena in liquid extraction. *Industrial and Engineering Chemistry*, *49*, 1030–1034. https://doi.org/10.1021/ie50570a038

Sigma-Aldrich. (2018). *1-heptanol and 1-nonanol manufacturer information*. Sigma-Aldrich.

Singh, P., & Joseph, D. D. (2005). Fluid dynamics of floating particles. *Journal of Fluid Mechanics*, *530*, 31–80. https://doi.org/10.1017/S0022112005003575

Smith, K. A. (1966). On convective instability induced by surface-tension gradients. *Journal of Fluid Mechanics*, *24*, 401–414. https://doi.org/10.1017/S0022112066000727

Spangenberg, W. G., & Rowland, W. R. (1961). Convective circulation in water induced by evaporative cooling. *The Physics of Fluids*, *4*, 743–750. https://doi.org/10.1063/1.1706392

Sternling, C. V., & Scriven, L. E. (1959). Interfacial turbulence: Hydrodynamic instability and the Marangoni effect. *AIChE Journal*, *5*, 514–523. https://doi.org/10.1002/aic.690050421

Sun, Z. F., Yu, K. T., Wang, S. Y., & Miao, Y. Z. (2002). Absorption and desorption of carbon dioxide into and from organic solvents: Effects of Rayleigh and Marangoni instability. *Industrial & Engineering Chemistry Research*, *41*, 1905–1913.

Thomson, J. (1855). On certain curious motions observable at the surfaces of wine and other alcoholic liquors. The London, Edinburgh, and Dublin Philosophical Magazine and. *Journal of Science*, *10*, 330–333.

Villers, D., & Platten, J. K. (1992). Coupled buoyancy and Marangoni convection in acetone: Experiments and comparison with numerical

simulations. *Journal of Fluid Mechanics*, *234*, 487–510. https://doi.org/10.1017/S0022112092000880

Wang, J.-M., Liu, G.-H., Fang, Y.-L., & Li, W.-K. (2016). Marangoni effect in nonequilibrium multiphase system of material processing. *Reviews in Chemical Engineering*, *32*, 551–558. https://doi.org/10.1515/revce-2015-0067

Wolf, K. L. (1959). *Physik und Chemie der Grenzflächen*. Springer.

Ye, C. W., & Li, J. (2012). Density, viscosity and surface tension of n-octanol-phosphoric acid solutions in a temperature range 293.15–333.15 K. *Russian Journal of Physical Chemistry*, *86*, 1515–1521. https://doi.org/10.1134/S0036024412100263

SUPPORTING INFORMATION

Additional supporting information can be found online in the Supporting Information section at the end of this article.